DE [redacted] ED

Copy

NASA TM X-127

NASA TM X-127

TECHNICAL MEMORANDUM
X-127

DECLASSIFIED BY AUTHORITY OF NASA
CLASSFICATION CHANGE NOTICES NO. 12
DATED 5-26-65 ITEM NO. 4

EFFECTS OF SIMULATED ROCKET-JET EXHAUST ON STABILITY AND CONTROL OF A RESEARCH-TYPE AIRPLANE CONFIGURATION AT A MACH NUMBER OF 6.86

By David E. Fetterman, Jr.

Langley Research Center
Langley Field, Va.

CLASSIFIED: EFFECTIVE 1-29-65
THORITY F.G. DROBKA (ATSS-A)
mo dated 5-13-65:AFSDO 5439

GPO PRICE $ ____________

OTS PRICE(S) $ ____________

Hard copy (HC) 2.00

Microfiche (MF) .50

[redacted] meaning

NATIONAL AERONAUTICS AND SPACE ADMINISTRATION
WASHINGTON October 1959

FACILITY FORM 602

N65 28135 (ACCESSION NUMBER)

(THRU)

36 (PAGES)

1 (CODE)

(NASA CR OR TMX OR AD NUMBER)

C4 (CATEGORY)

1A

DECLASSIFIED

[redacted]

NATIONAL AERONAUTICS AND SPACE ADMINISTRATION

TECHNICAL MEMORANDUM X-127

EFFECTS OF SIMULATED ROCKET-JET EXHAUST ON STABILITY AND CONTROL OF A RESEARCH-TYPE AIRPLANE CONFIGURATION AT A MACH NUMBER OF 6.86*

L
4
1
2

By David E. Fetterman, Jr.

SUMMARY

28135

An investigation has been undertaken in the Langley 11-inch hypersonic tunnel at a free-stream Mach number of 6.86 to determine the jet-interference effects at high jet-static-pressure ratios on the stability and control of a research-type airplane configuration. Compressed-air tests with a jet exhausting from the base of the fuselage were conducted over a Reynolds number range of 0.57×10^6 to 3.95×10^6, based on fuselage length, and over a jet-static-pressure-ratio range of 0 to 1460. The results of these tests indicated that the operation of the jet induced a sizeable separated-flow region over the vertical- and horizontal-tail surfaces which could be approximately duplicated at low angles of attack by use of metal jet-boundary simulators. The results of force tests, during which these metal jet-boundary simulators were used, indicated that this separated-flow region caused a large reduction in the longitudinal stability and control and a smaller reduction in the lateral and directional stability and control. By extending the divergent section of the nozzle and thus reducing the jet-static-pressure ratio, these losses were diminished.

AUTHOR

INTRODUCTION

Previous investigations have shown that a jet exhausting from the base of the fuselage may alter the base drag, the afterbody pressure distribution, and also the aerodynamic characteristics of the test configurations. (For example, see refs. 1 to 5.) High-performance and high-altitude aircraft will be subjected to these effects during the lower altitude portions of their trajectories. As the low ambient

---

*Title, Unclassified.

[redacted]

pressures associated with very high altitude are approached, however, jet-static-pressure ratios greatly exceeding those considered in previous investigations will be encountered. In order to determine the jet-interference effects which may occur at these high jet-static-pressure ratios and high Mach numbers, the investigation described in this paper was undertaken in the Langley 11-inch hypersonic tunnel at a Mach number of 6.86.

SYMBOLS

L
4
1
2

A_j	jet-exit plane area
A_t	jet throat area
b	wing span
C_D	drag coefficient, $\frac{\text{Drag}}{qS}$
C_L	lift coefficient, $\frac{\text{Lift}}{qS}$
C_l	rolling-moment coefficient, $\frac{\text{Rolling moment}}{qSb}$
C_m	pitching-moment coefficient, moment reference $0.20\bar{c}$, $\frac{\text{Pitching moment}}{qS\bar{c}}$
C_n	yawing-moment coefficient, $\frac{\text{Yawing moment}}{qSb}$
$\bar{c}$	wing mean aerodynamic chord
d_b	base diameter of fuselage
d_j	jet-exit diameter
l	fuselage length
M_j	jet-exit Mach number
M_∞	free-stream Mach number
p_j	jet static pressure
$p_{t,j}$	jet total pressure

[redacted]

p_∞	free-stream static pressure
q	dynamic pressure
R	Reynolds number, based on fuselage length
x_b	axial distance from base of fuselage
z	vertical distance from bottom of fuselage
z_t	lower vertical-tail span from bottom of fuselage measured at tail trailing edge-fuselage intersections (see fig. 8)
α	angle of attack
β	angle of sideslip
Δx	distance from fuselage base to jet exit
δ_h	horizontal-tail deflection, positive to produce positive C_L
$\delta_h{}'$	differential horizontal deflection, positive to produce positive C_l
δ_v	vertical-tail deflection, positive to produce negative C_n
γ_j	jet specific-heat ratio
θ_j	initial jet-boundary slope

L412

The following stability parameters are referred to the body axis system:

C_{n_β}	rate of change of yawing-moment coefficient with sideslip angle, $\partial C_n/\partial\beta$
C_{l_β}	rate of change of rolling-moment coefficient with sideslip angle, $\partial C_l/\partial\beta$
$C_{n_{\delta_v}}$	rate of change of yawing-moment coefficient with vertical-tail deflection, $\partial C_n/\partial\delta_v$
$C_{l_{\delta_v}}$	rate of change of rolling-moment coefficient with vertical-tail deflection, $\partial C_l/\partial\delta_v$

[redacted]

[redacted]

$C_{n_{\delta_h}}$'	rate of change of yawing-moment coefficient with differential horizontal-tail deflection, $\partial C_n/\partial \delta_h$'
$C_{l_{\delta_h}}$'	rate of change of rolling-moment coefficient with differential horizontal-tail deflection, $\partial C_l/\partial \delta_h$'

APPARATUS

Wind Tunnel

The tests were conducted in the Langley 11-inch hypersonic tunnel which is equipped with a single-step, two-dimensional nozzle constructed of Invar. Tunnel operation is of the intermittent type and a running time of about 80 seconds is possible. The nozzle was designed by the method of characteristics with a correction made for boundary layer and operates at an average Mach number of 6.86. The variation in Mach number after the first 10 seconds of running time is about 1 percent.

L
4
1
2

During these tests, the stagnation temperature was maintained at about 675° F by means of a variable-frequency, electrical heater equipped with Nichrome tube resistance elements. This high temperature is necessary to avoid air liquefaction in the test section. In order to eliminate the effects of water condensation, the absolute humidity of the air was kept less than 1.87×10^{-5} pounds of water vapor per pound of air for all tests.

Further details of the Langley 11-inch tunnel facility may be found in reference 6.

Balance and Force Model Support

Force and moment measurements were made through the use of a six-component-strain-gage force balance, the design of which allows four components to be located internally in the model. The other two components - axial force and rolling moment - are mounted externally at the rear of the balance and are shielded from the air flow during the test runs. The model and balance were mounted in the test section on a movable support strut which could be rotated through an angle-of-attack range. During each test, the period of essentially constant Mach number flow was long enough to permit testing through the angle-of-attack range. Angles of sideslip were obtained by offsetting the model and balance support to the desired sideslip angle prior to each run. Thus, the data were obtained at an essentially constant sideslip angle over an angle-of-attack range.

[redacted]

[redacted]

Models

Force-test model.- A three-view drawing of the model used for the force test of this investigation is presented in figure 1, and the geometric characteristics are given in table I. The model consisted of a slightly boattailed, ogive-cylinder combination with side fairings, a trapezoidal wing, swept horizontal-tail surfaces, and swept lower and upper vertical-tail surfaces.

L
4
1
2

The horizontal-tail panels are deflected together for pitch control and differentially for roll control. The inboard portions of the vertical tail are fixed and support the speed brakes, details of which are shown in figure 2. The outboard portions of the vertical tail are deflected for directional control.

Compressed-air-test model.- A sketch showing the construction details and pertinent dimensions of the model used in the compressed-air test to obtain the extent of the jet-interference flow field and the jet-boundary shapes is presented in figure 3. The model was made of stainless steel and the exterior surfaces were smooth. The fuselage, which is identical to that of the force-test model previously described, is supported on the right side by an 8.75-percent-thick support strut from the tunnel side wall. This strut contained copper air-supply tubes and the jet-stagnation-pressure tube. The strut was extended from the left side of the fuselage far enough to permit a symmetrical flow field on each side of the fuselage. Dry air at 2000 lb/sq in. from a storage tank was used as the jet exhaust gas and was piped through a throttling valve into the air-supply tubes at approximately atmospheric temperature. The jet stagnation pressures were measured in a small offset chamber ahead of the jet-stagnation-pressure chamber as shown in figure 3. By employing this arrangement little, if any, effect of the flow velocity in the jet-stagnation-pressure chamber was obtained in the recorded stagnation pressures.

Nozzles.- The majority of the compressed-air tests were made by using the nozzle A configuration shown in figure 4. This nozzle is a supersonic, convergent-divergent, conical nozzle having a semidivergence angle of 20°. A limited number of tests were also made with nozzles B and C, also shown in figure 4, which were essentially identical to nozzle A except that the divergent sections of these nozzles were extended so that their exit planes were at different distances from the base of the fuselage. These nozzles were used to determine the effects of nozzle extensions. All three nozzles were designed on the basis of area ratio only for $\gamma_j = 1.25$. However, in altering the design of the nozzles for use with air ($\gamma_j = 1.4$) so that the correct values of M_j, d_j/d_b, and $\Delta x/d_b$ were maintained, the resulting throat diameters of

[redacted]

[redacted]

the nozzles were not constant. Pertinent information concerning these nozzles is given in the following table:

Nozzle	M_j	d_j/d_b	$\Delta x/d_b$	A_j/A_t
A	3.40	0.556	0.082	6.184
B	3.93	.785	.393	10.07
C	4.21	.927	.592	12.90

L
4
1
2

A typical installation of nozzle A in the compressed-air-test model is shown in figure 3.

Nozzle A was calibrated by obtaining total-head-pressure measurements across the nozzle exit plane. The average Mach number obtained from the measured ratio of total head to stagnation pressures varied not more than ±0.01 from the average design jet Mach number. Nozzles B and C could not be calibrated with atmospheric jet-exit pressure because sufficiently high jet-supply pressure was not available to start the nozzles completely.

TESTS

All tests were conducted at a free-stream Mach number of 6.86. An off axis, single-pass, two-mirror, schlieren system utilizing a mercury-vapor light source was used during all tests. Schlieren photographs were recorded on standard panchromatic film exposed for approximately 1/150 sec.

Compressed-Air Tests

The compressed-air tests with nozzle A in place were made at tunnel stagnation pressures of 5, 10, 17.5, and 34 atmospheres. These stagnation pressures in combination with the free-stream Mach number of 6.86 and stagnation temperature of 675° resulted in Reynolds numbers, based on fuselage length, of 0.57×10^6, 1.20×10^6, 2.05×10^6, and 3.95×10^6, respectively. Because of the limited capacity of the nozzle high-pressure air supply and the accompanying losses in the air-supply piping, the maximum jet-static-pressure ratios obtainable varied with different test Reynolds numbers. These maximum jet-static-pressure ratios and also

[redacted]

the test angles of attack for the various nozzle and Reynolds number combinations are given in the following table:

Nozzle	R	$(p_j/p_\infty)_{max}$ for $\gamma_j = 1.4$	α, deg
A	0.57×10^6	1460	0
	1.20	528	0, ±2, ±4
	2.05	450	0
	3.95	215	0
B	2.05×10^6	170	0
C	2.05×10^6	139	0

Force Tests

Six-component force and moment data at Reynolds numbers of 1.20×10^6 and 2.05×10^6 were obtained with all controls undeflected for an angle-of-attack range of $\pm 4^\circ$ and sideslip angles of 0° and 4°. At $\beta = 0^\circ$ the model was also tested with the vertical tails deflected -5° and also a differential horizontal-tail deflection of 10°. The angles of attack were set using a lens prism imbedded in the model surface to reflect and focus a spot from a light source onto a previously calibrated screen. By using this method the true angles of attack were obtained directly, irrespective of balance deflection under load.

Precision of Data

The probable uncertainties in the force and moment coefficients due to balance repeatability have been estimated and are presented as follows:

C_L	±0.005
C_D	±0.001
C_m	±0.003
C_n	±0.0005
C_l	±0.0003

The accuracy of α and β was within the limits of $\pm 0.10^\circ$.

[redacted]

[redacted]

JET SIMULATION TECHNIQUE

Simulation of Initial Jet-Boundary Slope

A typical variation of jet-static-pressure ratios p_j/p_∞ with altitude for the case of $\gamma_j = 1.25$, which is intended to simulate hot gases being expelled from the nozzles, is presented in figure 5 for the three nozzles under consideration. In calculating these curves a jet-stagnation-chamber pressure of 600 lb/sq in. was assumed. Indicated in figure 5 at an altitude of about 158,000 feet are the jet-static-pressure ratios which were simulated during the force tests of this investigation. For nozzle A, $p_j/p_\infty = 420$; for nozzle B, $p_j/p_\infty = 170$; and for nozzle C, $p_j/p_\infty = 105$.

L
4
1
2

Since air ($\gamma_j = 1.4$) instead of a hot gas ($\gamma_j = 1.25$) was used as the exhaust medium, it was necessary to test at equivalent air-jet static-pressure ratios so that the initial jet-boundary slope could be reasonably duplicated. The effect of specific-heat ratio of the initial boundary slope of the jet from nozzle A is shown in figure 6 for specific-heat ratios of 1.25 and 1.40. In calculating these curves, the flow over the afterbody was assumed to be attached and two-dimensional-oblique-shock and expansion relations were used in the manner suggested in references 7 and 8. As seen from figure 6, increasing the specific-heat ratio from 1.25 to 1.40 causes a considerable reduction in the initial jet-boundary slope; therefore, in order to duplicate the jet-boundary slope which would occur under hot-jet gas conditions, a higher equivalent air-jet static-pressure ratio is required. For example, in order to duplicate the jet-boundary slope at a hot gas-jet static-pressure ratio of 420, it was necessary to use an equivalent air-jet static-pressure ratio of 1,200 during the compressed-air tests.

It should be noted that in computing the jet-static-pressure ratios presented herein, a straightforward two-dimensional approach, based on the perfect gas law, was used to calculate the nozzle exit pressures; however, because of the high jet stagnation pressures encountered at the higher values of p_j/p_∞, some departure from the perfect gas assumption does exist. Furthermore, because of the large area ratios for the extended nozzles, some air liquefaction probably occurred within nozzles B and C. However, since this investigation was intended to determine only the general trends of jet-interference effects at high jet-static-pressure ratios, no attempt was made to correct the jet-static-pressure ratios for these effects.

[redacted]

Simulation of Jet-Interference Flow Field

Schlieren photographs of the flow field produced by the compressed-air jet indicated that the pressure rise produced by the jet-exit shock was sufficient to induce a separated-flow region which extended over and forward from the rearward end of the fuselage. This jet-induced separated-flow region may be seen in figure 7(a) in which a schlieren photograph of the flow field produced by the air jet from nozzle A exhausting into a Mach number 6.86 air stream is presented. Because of the orientation of the schlieren knife edge, the separated-flow-region boundary can be seen directly only over the lower surface of the model; however, the location over the upper surface is indicated by the discontinuity of the jet boundary and the point of origin of the jet-exit shock. It should be noted that the jet boundary is asymmetrical, and the larger separated-flow region occurs over the lower portion of the fuselage. The reason for this behavior will be discussed in a subsequent section.

In view of the rather large area covered by this jet-induced separated-flow region, it was believed that significant jet-exhaust effects would result from the presence of this separated-flow region over a large portion of the fuselage and the conventionally located tail-control surfaces. The jet-simulation technique employed consisted of inducing these separated-flow regions over the rearward end of the force-test model. This was accomplished by mounting metal jet-boundary simulators on the windshield of the force balance just aft of the model. It was necessary, however, to neglect the jet-boundary asymmetry, since the attainment of the shape and the fabrication of asymmetrical jet-boundary simulators was impractical. Instead, a symmetrical jet boundary was approximated through the use of axisymmetric, metal jet-boundary simulators which were machined to the lower-surface jet-boundary shapes at $\alpha = 0^{\circ}$ obtained from schlieren photographs of the compressed-air tests. When it was necessary, these metal fairings were then modified by a reduction in the length of the jet-boundary simulator to produce approximately the same lower-surface separated-flow regions at an angle of attack of 0° as those obtained from the compressed-air tests. In figure 7(b) the separated-flow region produced by one of these jet-boundary simulators is shown. This jet-boundary simulator has been modified to induce the same lower-surface separated-flow region as that induced by the air jet (fig. 7(a)) and is the only one of the three jet-boundary simulators tested which required modification.

A better comparison of the lower-surface separated-flow regions induced by the air jet and the jet-boundary simulator is shown in figure 8. In this figure the extent of the separated-flow regions are shown in terms of the parameter z/z_t in which z is the height of the separated-flow region and z_t is the height of the lower vertical tail.

[redacted]

[redacted]

At $\alpha = 0^{\circ}$ it is seen from the figure that the jet-boundary simulator induces a very nearly identical separated-flow region to that induced by the air jet. At angles of attack, however, the actual jet-boundary shape changes so that a decrease occurs in the extent of the separated-flow region on the high-pressure side of the configuration with increasing angle of attack. As mentioned previously, it was impractical to obtain the true jet-boundary shape and to construct asymmetrical metal jet-boundary simulators for each angle of attack; therefore, the zero angle-of-attack jet-boundary simulators were used throughout the test angle-of-attack range. Comparisons of the lower-surface separated-flow regions induced at 2° and 4° angle of attack by the air-jet and jet-boundary simulator are also shown in figure 8. These comparisons indicate that at angles of attack, the jet-boundary simulator induces a progressively larger separated-flow region than does the air jet. A reversal of these trends would be expected to occur on the low-pressure side of the configuration. In view of these results, then, the angle-of-attack range of the force tests was limited to $\pm 4^{\circ}$.

RESULTS AND DISCUSSION

Compressed-Air Tests

Representative schlieren photographs which show the flow field at $\alpha = 0^{\circ}$ produced by the air jet at various values of p_j/p_∞ and Reynolds number are presented in figure 9. The pictures for the jet off are included to show the location of the shock waves and wake from the model-support strut. In the photographs for $p_j/p_\infty > 0$, the jet-induced separated-flow regions are indicated, and these, again, can be seen directly only over the lower surface of the fuselage. It should be noted that for all values of p_j/p_∞, the jet boundary is asymmetrical and the larger separated-flow regions occur over the lower surface of the fuselage. Tests with the canopy removed (see fig. 9(b)) indicate that this behavior was due to the asymmetrical flow field about the fuselage caused by the presence of the canopy.

The effects of equivalent air-jet static-pressure ratio and Reynolds number on the extent of this jet-induced separated-flow region over the lower surface of the fuselage at $\alpha = 0^{\circ}$ are shown in figure 10. The parameter z/z_t is again used to indicate the extent of the separated-flow region; however, in this figure, z is the height of the separated-flow region at the base of the fuselage. At the lower Reynolds numbers the separated-flow region increases rapidly with jet-static-pressure ratio, and for a Reynolds number of 0.57×10^6 and jet-static-pressure ratios greater than 1,000 the separated-flow region covers the entire lower vertical tail. At a constant jet-static-pressure ratio, however,

[redacted]

the extent of the separated-flow region decreases rapidly with increasing Reynolds number. The values of z/z_t for $p_j/p_\infty = 0$ are really the boundary-layer thicknesses at the various Reynolds numbers with the jet off.

A Reynolds number of 2.05×10^6 was chosen for the nozzle B and nozzle C compressed-air tests and also for the ensuing force tests. For nozzle A, the equivalent air-jet-static-pressure ratio of 1,200 at a Reynolds number of 2.05×10^6 corresponds to the hot-gas-jet value of 420. (See fig. 6.) Since the jet-air supply pressure was insufficient to permit testing at this equivalent jet-static-pressure ratio and Reynolds number combination, extrapolations of the available data, indicated by the dashed lines, were made by using the lower Reynolds number variation as a guide to determine the separated-flow conditions that would exist for nozzle A. Similar extrapolations of the available data were also necessary for nozzle B and nozzle C. These extrapolated separated-flow conditions for the various nozzles are indicated by the solid symbols. Since the flow from nozzles B and C is underexpanded to a lesser degree than that from nozzle A, the extent of the separated-flow regions for these nozzles is less than for nozzle A.

Since a determination of the separated-flow region induced by nozzle A could not be obtained experimentally at the required equivalent jet-static-pressure-ratio and Reynolds number combination it was necessary to use the available experimental data at $p_j/p_\infty = 528$ and at a reduced Reynolds number of 1.20×10^6, which figure 10 shows closely approximated the desired separated-flow conditions. The schlieren photograph from this test shown in figure 7(a) was used for defining the jet-boundary-simulator shape for nozzle A used during the force tests.

Force Tests

The effects produced by this simulated-jet-exhaust technique on the longitudinal characteristics of the test configuration are shown in figure 11 in which the variations of C_D and α with C_L are presented for the jet off and with the jet-boundary simulators for nozzle A, nozzle B, and nozzle C in place. These data show that the presence of the jet exhaust reduced both the lift-curve slope C_{L_α} and the minimum drag coefficient from the jet-off values. This reduction in C_{L_α} can be attributed to the loss in the lift contributions of those portions of the horizontal-tail surfaces and fuselage which are submerged within the low-energy flow of jet-induced separated-flow regions. The largest reduction in C_{L_α}, about 20 percent, occurred for nozzle A, which would be expected since as noted in figure 10 the jet boundary from this nozzle

[redacted]

induced the largest separated-flow region. The reduction in minimum drag coefficient, also about 20 percent, was the same for all three nozzles tested and was probably due to an increase in base and afterbody pressures over those present with the jet off.

The longitudinal stability and control results are shown in figure 12 in which the variation in pitching-moment coefficient with lift coefficient is presented for horizontal-tail deflections of 0° and -20°. In considering first the curves for $\delta_h = 0^\circ$ with the jet off, the configuration is seen to be statically stable with a static margin of about 13 percent of the mean aerodynamic chord. Under the influence of the separated-flow region from the jet simulator for nozzle A, however, the configuration is statically unstable over a small positive and negative lift-coefficient range. Because of the smaller separated-flow regions induced with the extended nozzles B and C, less losses in longitudinal stability occur.

The effects of the simulated-jet exhaust on the longitudinal control power of the horizontal tail are indicated by the difference in the curves for $\delta_h = 0^\circ$ and $\delta_h = -20^\circ$. With the jet off, some loss in control power occurs at negative lift coefficients because of wing-wake impingement on the horizontal tails. This behavior was previously observed in the investigation reported in reference 9. The combination of the wing wake and jet-induced separated-flow region from the jet simulator for nozzle A, however, causes a large reduction in control power so that at negative lift coefficients, the horizontal tail becomes almost ineffective. With the extended nozzles B and C, the control power at negative lift coefficients is reduced only about 15 percent below that with the jet off.

As pointed out previously and as indicated in figures 11 and 12, the tests with the nozzle A jet-boundary simulator in place were conducted at a reduced Reynolds number of 1.20×10^6. In order to determine what effect this reduction in Reynolds number had on the foregoing curves for nozzle A, the model with the jet off was also tested at this reduced Reynolds number. The results of this test are compared with the jet-off data at a Reynolds number of 2.05×10^6 in figure 13. These comparisons indicate no Reynolds number effect on the longitudinal characteristics when $\delta_h = 0^\circ$. For $\delta_h = -20^\circ$, however, the lower Reynolds number results show a loss in control power; nevertheless, this loss is not nearly as large as that indicated by the curves for nozzle A in figure 12. In view of these results, then, the deviations from the jet-off characteristics indicated by the curves for nozzle A in figures 11 and 12 can reasonably be attributed to the influence of the jet-induced separated-flow region.

[redacted]

Contrary to this trend, little, if any, changes occurred between the jet-off and jet-on conditions in the lift and pitching-moment characteristics of the configuration with the speed brakes deflected 35°. These results are shown in figure 14. The minimum drag coefficient under the jet-on conditions, however, was again reduced about 20 percent below the jet-off value. The jet-on results are presented only for nozzle A since almost identical results were obtained with nozzles B and C. Since the characteristics of speed brakes of the type used on the configuration are affected to a large extent by Reynolds number, both the jet-off and jet-on data of this figure are presented for a Reynolds number of 1.20×10^6.

L
4
1
2

For the directional stability and control results presented in figure 15, losses are seen to occur in both C_{n_β} and $C_{n_{\delta_V}}$ due to the effects of the simulated-jet exhaust from nozzle A. By extending the nozzle divergent section (nozzles B and C) these losses are diminished so that no change in C_{n_β} and only about a 6-percent reduction in $C_{n_{\delta_V}}$ occurs.

The lateral stability and control results are shown in figure 16 which also indicates an unfavorable contribution to the effective dihedral parameter C_{l_β} at positive values of α and a reduction in the rolling-tail-control parameter $C_{l_{\delta_h}}$, due to the effects of the simulated jet from nozzle A. Smaller reductions in these parameters were again obtained with nozzles B and C.

The curves presented in figures 15 and 16 summarize the significant simulated-jet-exhaust effects on the lateral and directional stability and control obtained during this investigation. The model was also tested at the reduced Reynolds number of 1.20×10^6 and also with the speed brakes deflected 35°; however, these data showed no noticeable change in the lateral and directional stability and control characteristics between the simulated-jet-on and jet-off conditions.

Full-Scale Considerations

In view of the foregoing results, one question which might naturally arise is whether these simulated-jet-exhaust effects are truly representative of those which may be encountered during an actual flight. In answering, it must be noted that during this investigation, schlieren photographs indicated that the boundary layer was laminar over the full length of the fuselage and various attempts to induce transition artificially were unsuccessful. On a full-scale vehicle, however, boundary-layer transition may very likely occur ahead of the tail surfaces; thus

[redacted]

the jet-induced separated-flow regions and consequently the jet-interference effects would be expected to be smaller. Therefore, although the use of this simulated-jet-exhaust technique may not predict the exact magnitude of these effects, it is believed that these results are useful for indicating trends and pointing out problem areas which should be considered in the design of high-altitude, high-performance aircraft.

CONCLUDING REMARKS

L412

An investigation has been conducted in the Langley 11-inch hypersonic tunnel at a free-stream Mach number of 6.86 to determine the jet-interference effects at high jet-static-pressure ratios on the stability and control of a research-type airplane configuration.

The results of this investigation indicated that the jet-exhaust boundary induced a considerable separated-flow region in the vicinity of the tail surfaces, the extent of which increased with jet-static-pressure ratio and decreased with an increase in Reynolds number.

A jet-interference-field-simulation technique was developed which approximated the jet-induced separated-flow region over the test configuration at low angles of attack. The results obtained with this simulated jet-exhaust technique indicated that the separated-flow region caused a large reduction in the longitudinal stability and control and a smaller reduction in the lateral and directional stability and control. By extending the divergent section of the nozzle, and thus reducing the jet-static-pressure ratio, these losses were diminished.

Langley Research Center,
National Aeronautics and Space Administration,
Langley Field, Va., July 27, 1959.

[redacted]

REFERENCES

1. Cortright, Edgar M., Jr., and Schroeder, Albert H.: Investigation at Mach Number 1.91 of Side and Base Pressure Distribution Over Conical Boattails Without and With Jet Flow Issuing From Base. NACA RM E51F26, 1951.

2. Cortright, Edgar M., Jr., and Kochendorfer, Fred D.: Jet Effects on Flow Over Afterbodies in Supersonic Stream. NACA RM E53H25, 1953.

L412

3. Love, Eugene S.: Aerodynamic Investigation of a Parabolic Body of Revolution at Mach Number of 1.92 and Some Effects of an Annular Supersonic Jet Exhausting From the Base. NACA TN 3709, 1956. (Supersedes NACA RM L9K09.)

4. Bromm, August F., Jr., and O'Donnell, Robert M.: Investigation at Supersonic Speeds of the Effect of Jet Mach Number and Divergence Angle of the Nozzle Upon the Pressure of the Base Annulus of a Body of Revolution. NACA RM L54I16, 1954.

5. Grigsby, Carl E.: An Investigation of the Effects of Jet Exhaust and Reynolds Number Upon the Flow Over the Vertical Stabilizer and Rudder of the Douglas D-558-II Research Airplane at Mach Numbers of 1.62, 1.93, and 2.41. NACA RM L54E03, 1954.

6. McLellan, Charles H., Williams, Thomas W., and Beckwith, Ivan E.: Investigation of the Flow Through a Single-Stage Two-Dimensional Nozzle in the Langley 11-Inch Hypersonic Tunnel. NACA TN 2223, 1950.

7. Love, Eugene S.: Initial Inclination of the Mixing Boundary Separating An Exhausting Supersonic Jet From a Supersonic Ambient Stream. NACA RM L55J14, 1956.

8. Love, Eugene S., Woodling, Mildred J., and Lee, Louise P.: Boundaries of Supersonic Axisymmetric Free Jets. NACA RM L56G18, 1956.

9. Penland, Jim A., Fetterman, David E., Jr., and Ridyard, Herbert W.: Static Longitudinal and Lateral Stability and Control Characteristics of an Airplane Configuration Having a Wing of Trapezoidal Plan Form With Various Tail Airfoil Sections and Tail Arrangements at a Mach Number of 6.86. NACA RM L55F17, 1955.

[redacted]

TABLE I

GEOMETRIC CHARACTERISTICS OF MODEL

Wing:	
Area, total, sq in.	11.520
Area, exposed, sq in.	6.050
Span, in.	5.366
Aspect ratio	2.500
Root chord, in.	3.578
Root chord, exposed, in.	2.640
Tip chord, in.	0.716
Mean aerodynamic chord, in.	2.465
Sweepback angles -	
Leading edge, deg	36.75
25-percent element, deg	25.64
Trailing edge, deg	-17.74
Taper ratio	0.200
Dihedral angle, deg	0.00
Incidence angle, deg	0.00
Airfoil section (parallel to fuselage center line)	NACA 66005 (modified)
Horizontal tail:	
Area, total, sq in.	6.643
Area, exposed, sq in.	2.878
Span, in.	4.339
Aspect ratio	2.833
Taper ratio	0.206
Root chord, exposed, in.	1.658
Tip chord, in.	0.506
Mean aerodynamic chord, exposed, in.	1.184
Sweepback angles -	
Leading edge, deg	50.58
25-percent element, deg	45.00
Trailing edge, deg	19.28
Dihedral, deg	-15.000
Airfoil section (parallel to fuselage center line)	NACA 66005 (modified)
Upper vertical tail:	
Area, exposed, sq in.	2.356
Span, exposed, in.	1.099
Aspect ratio	0.516
Taper ratio	0.741

L
4
1
2

[redacted]

TABLE I.- Concluded

GEOMETRIC CHARACTERISTICS OF MODEL

Root chord, in.	2.450
Tip chord, in.	1.815
Mean aerodynamic chord, in.	2.148
Sweepback angles -	
Leading edge, deg	30.000
25-percent element, deg	23.413
Trailing edge, deg	0.000
Airfoil section (parallel to fuselage center line)	10° full wedge
Leading-edge radius, in.	0.010
Area, control surface, in.	1.523
Root chord, control surface, in.	2.248
Mean aerodynamic chord, control surface, in.	2.039
Lower vertical tail:	
Area, sq in.	1.982
Span, exposed, in.	0.920
Aspect ratio	0.429
Taper ratio	0.783
Root chord, in.	2.450
Tip chord, in.	1.919
Mean aerodynamic chord, in.	2.200
Sweepback angles -	
Leading edge, deg	30.000
25-percent element, deg	23.413
Trailing edge, deg	0.000
Airfoil section (parallel to fuselage center line)	10° full wedge
Leading-edge radius, in.	0.010
Area, control surface, in.	1.149
Root chord, control surface, in.	2.248
Mean aerodynamic chord, control surface, in.	2.093
Fuselage:	
Length, in.	11.76
Maximum diameter, in.	1.12
Maximum width (including side fairings), in.	1.76
Fineness ratio	10.50
Base diameter	0.960

[redacted]

[redacted]

[redacted]

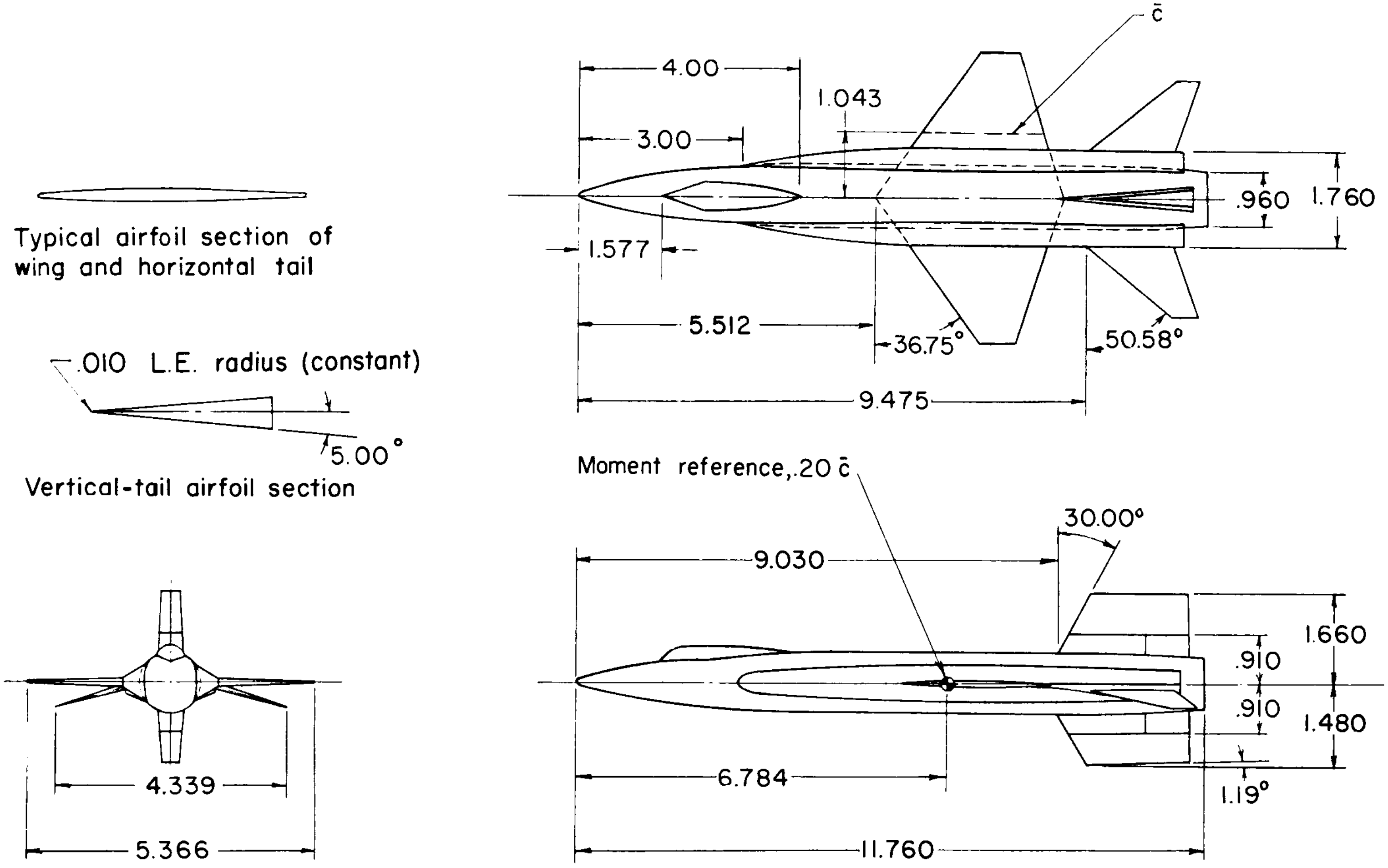

Figure 1.- Details of the force model. All dimensions are in inches.

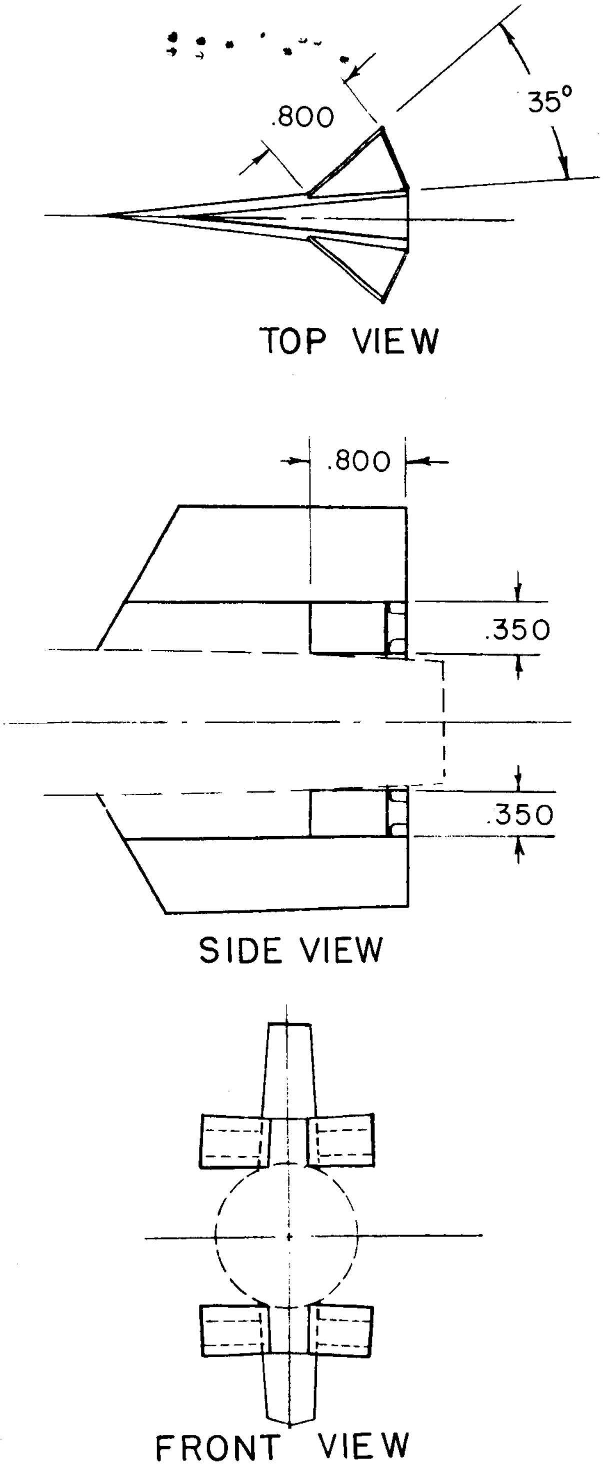

Figure 2.- Details of the speed brakes. All dimensions are in inches.

[redacted]

[redacted]

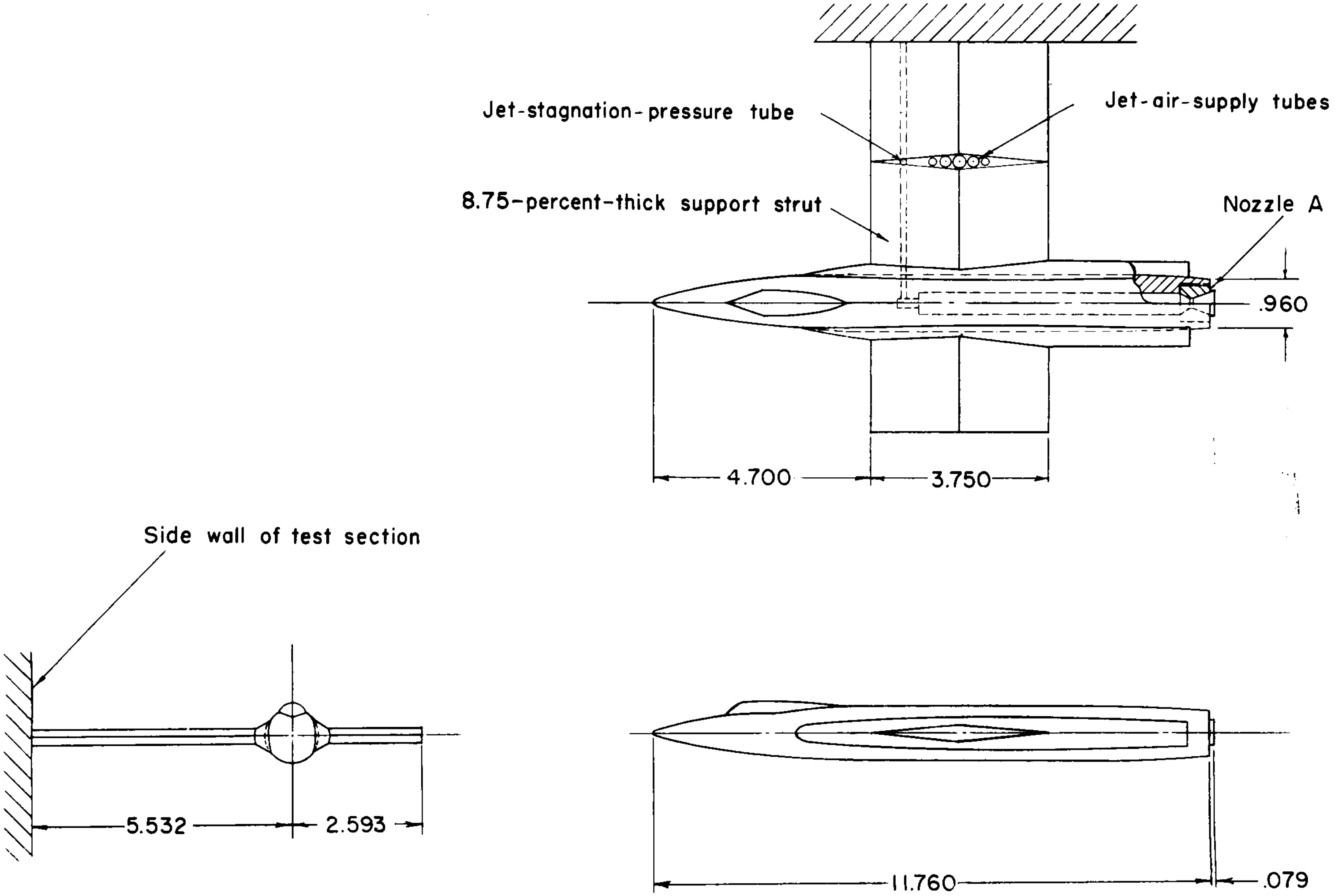

Figure 3.- Details of the compressed-air model. All dimensions are in inches.

[redacted]

[redacted]

L-412

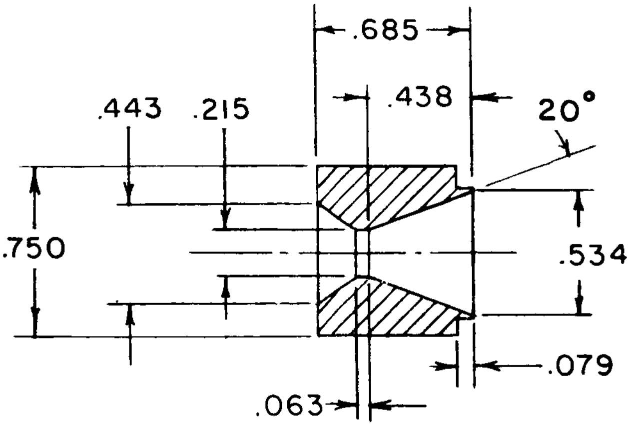

Nozzle A

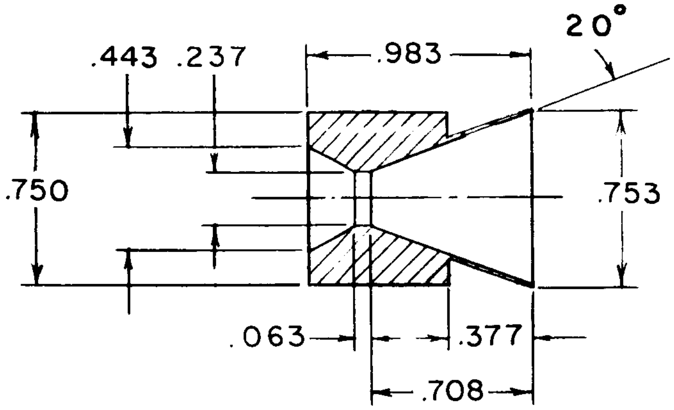

Nozzle B

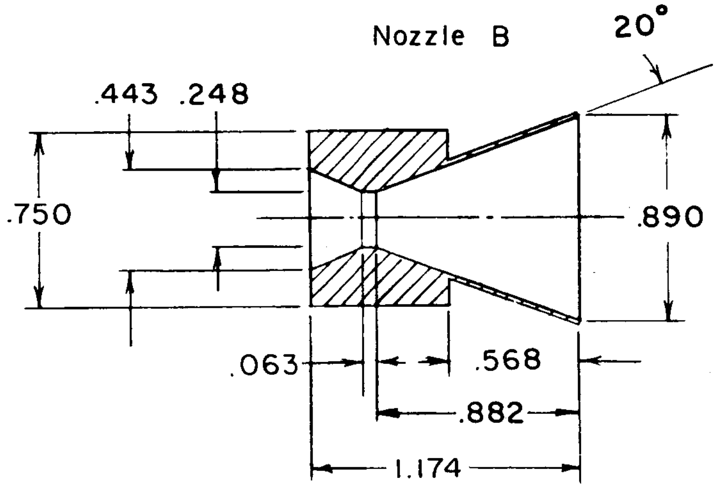

Nozzle C

Figure 4.- Details of the nozzle configurations. All dimensions are in inches.

[redacted]

[redacted]

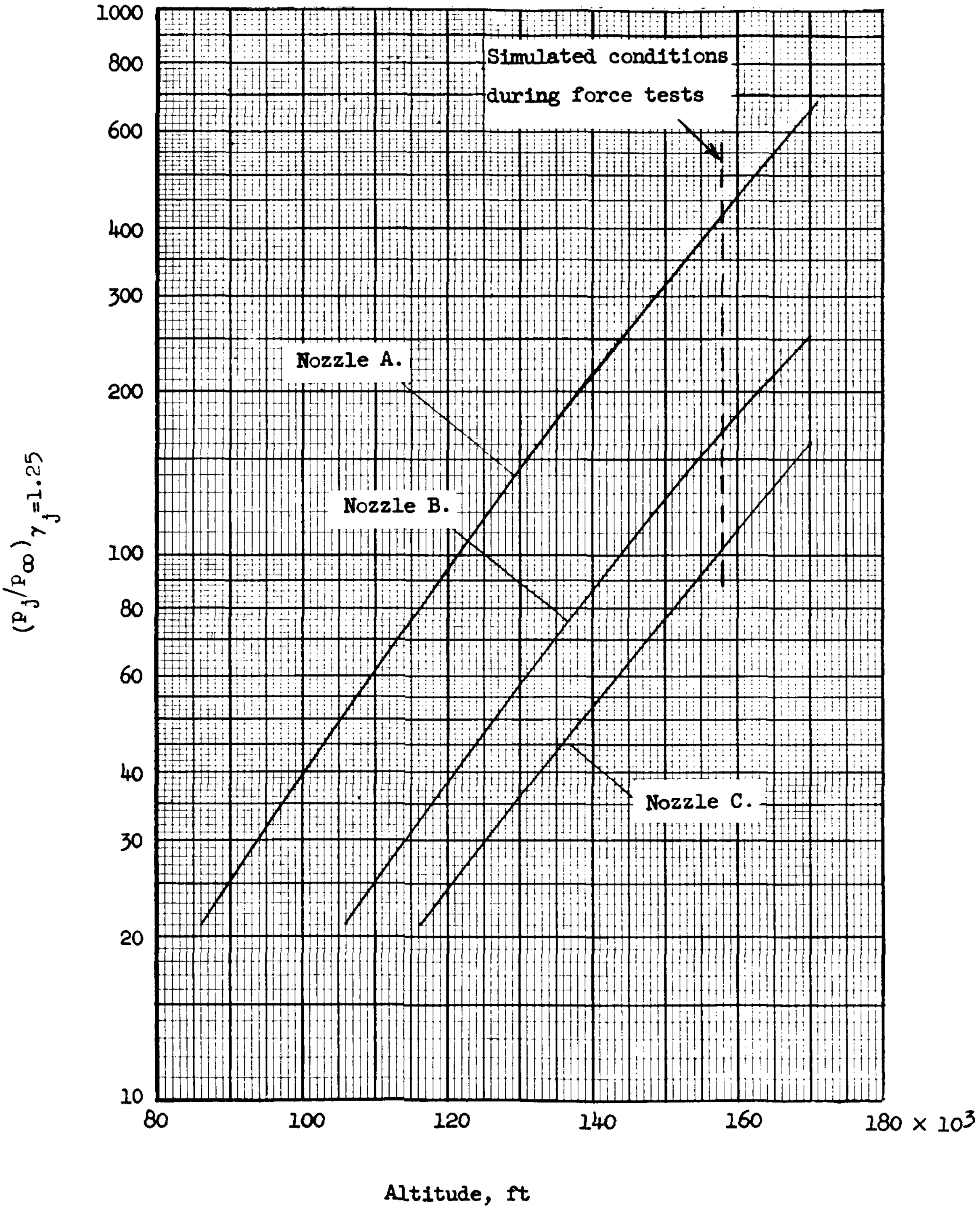

Figure 5.- Effect of altitude on jet-static-pressure ratio. $p_{t,j}$ = 600 lb/sq in.; γ_j = 1.25.

L-412

[redacted]

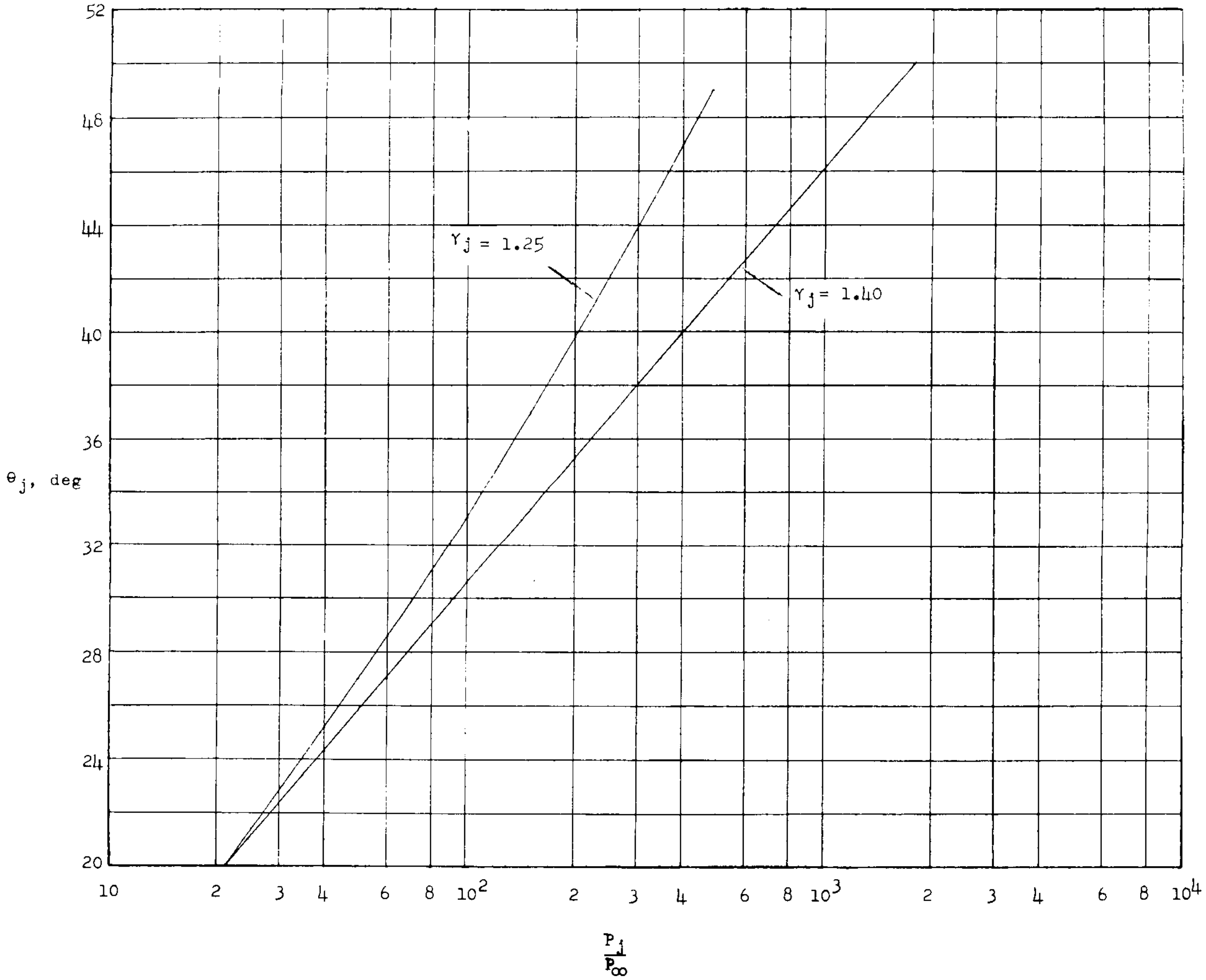

Figure 6.- Effect of jet specific-heat ratio on initial jet-boundary slope from nozzle A. $M_\infty = 6.86$; $M_j = 3.40$.

DECL[redacted]IED

[redacted]

[redacted]

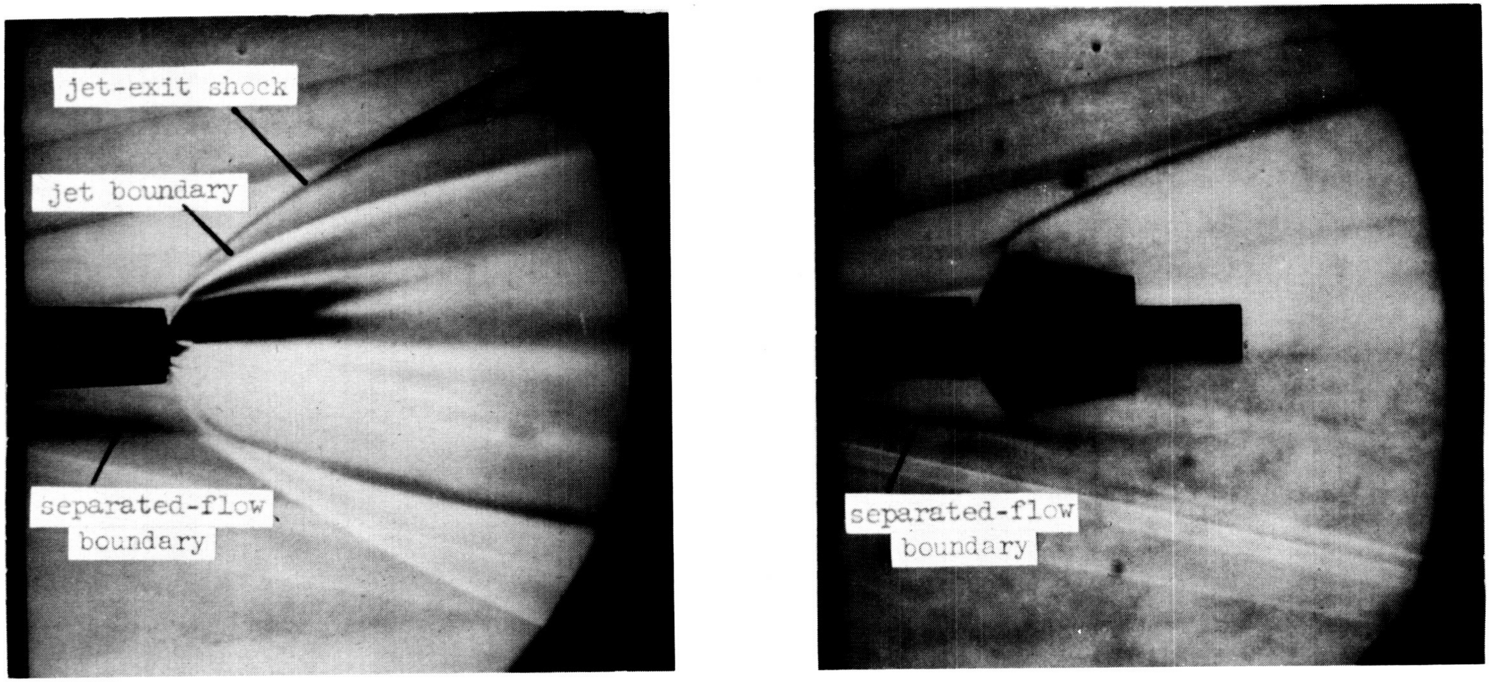

(a) Air jet.

(b) Jet-boundary simulator. L-59-5007

Figure 7.- Flow fields produced by the air jet from nozzle A and metal jet-boundary simulator. $\alpha = 0^{\circ}$; $M_{\infty} = 6.86$; $R = 1.20 \times 10^{6}$; $\left(p_j/p_{\infty}\right)_{\gamma_j=1.4} = 528$.

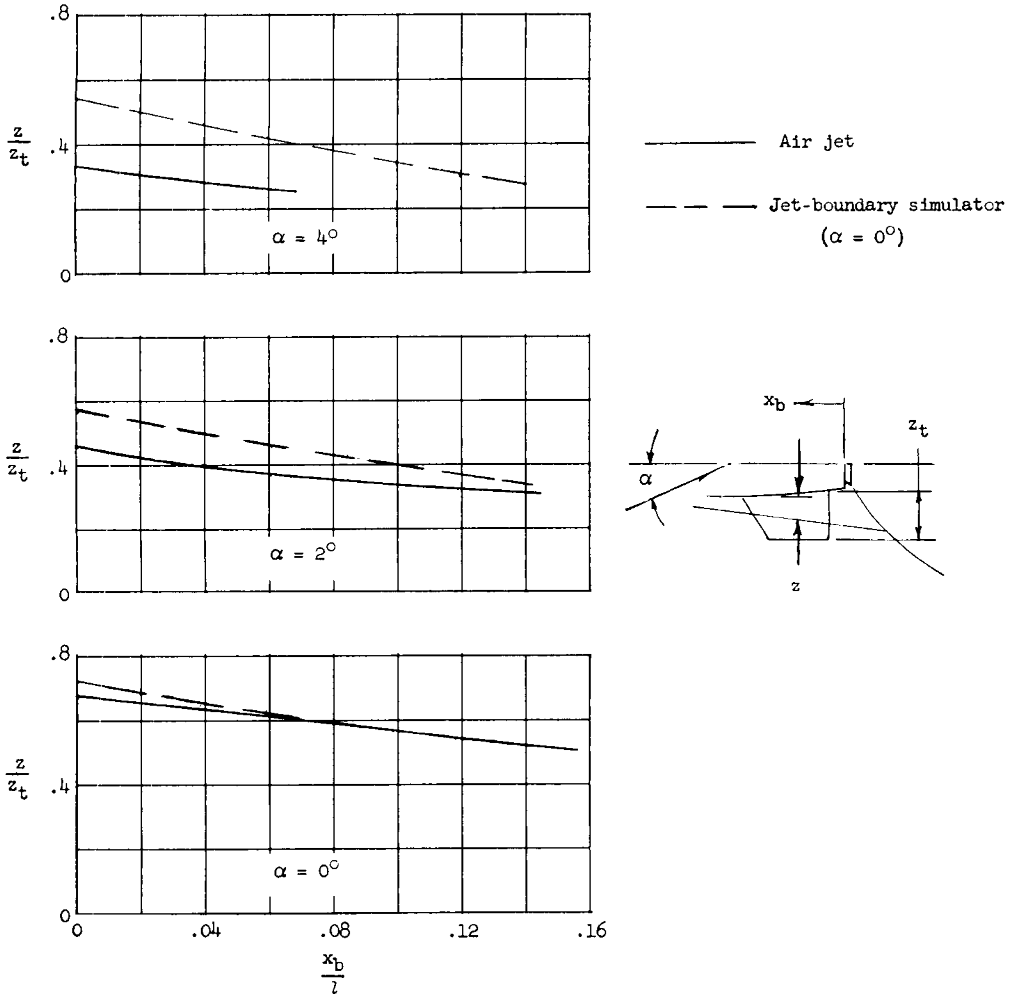

Figure 8.- Separated-flow regions induced by air jet from nozzle A and jet-boundary simulator. $M_\infty = 6.86$; $R = 2.05 \times 10^6$; $(p_j/p_\infty)_{\gamma_j=1.4} = 528$.

[redacted]

[redacted]

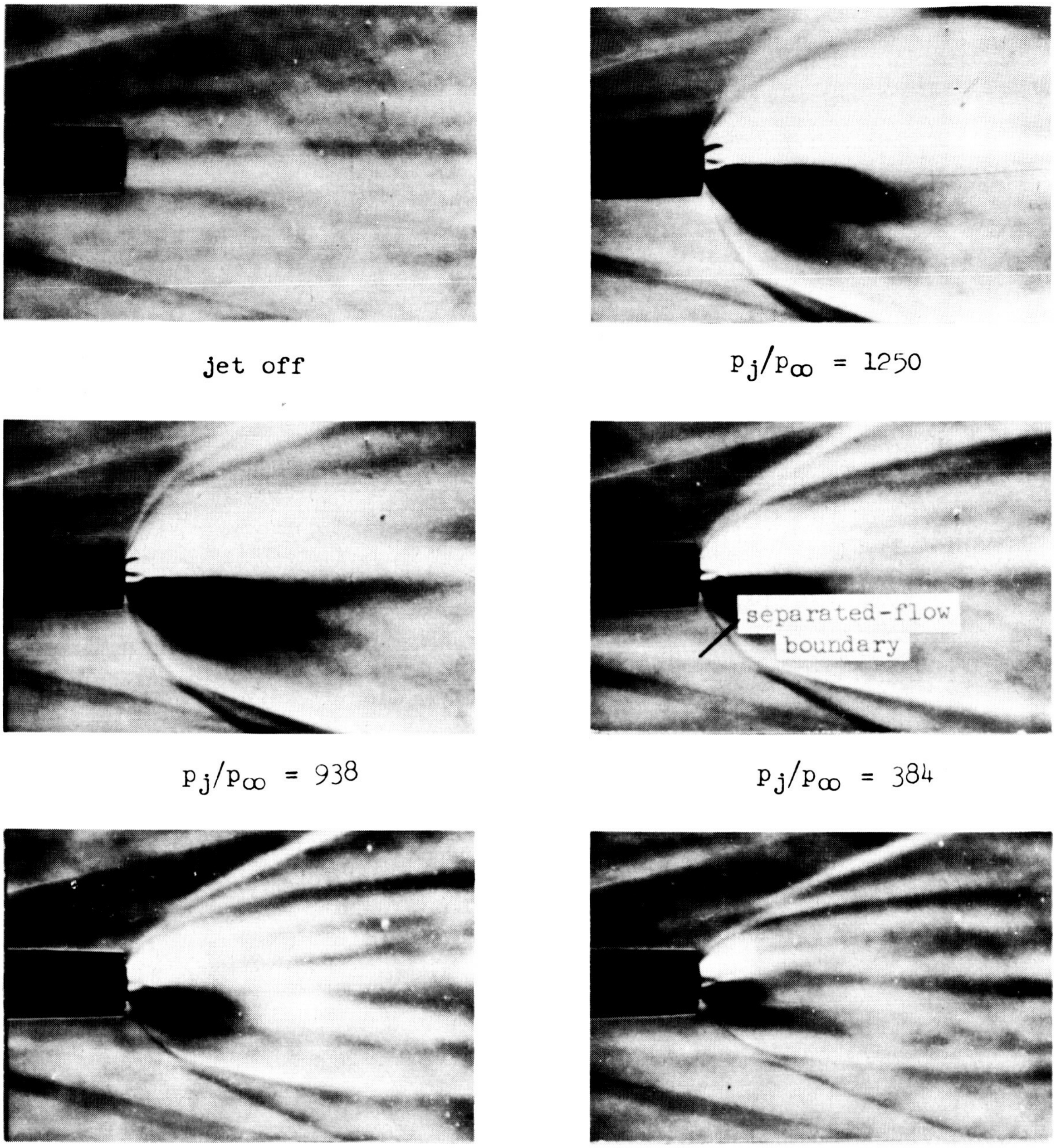

jet off

p_j/p_∞ = 1250

p_j/p_∞ = 938

p_j/p_∞ = 384

p_j/p_∞ = 192

p_j/p_∞ = 107

(a) Nozzle A; $R = 0.57 \times 10^6$. L-59-5008

Figure 9.- Schlieren photographs of the flow fields produced by the air jet at various values of p_j/p_∞ and Reynolds number. $\alpha = 0^\circ$; $M_\infty = 6.86$.

[redacted]

L-412

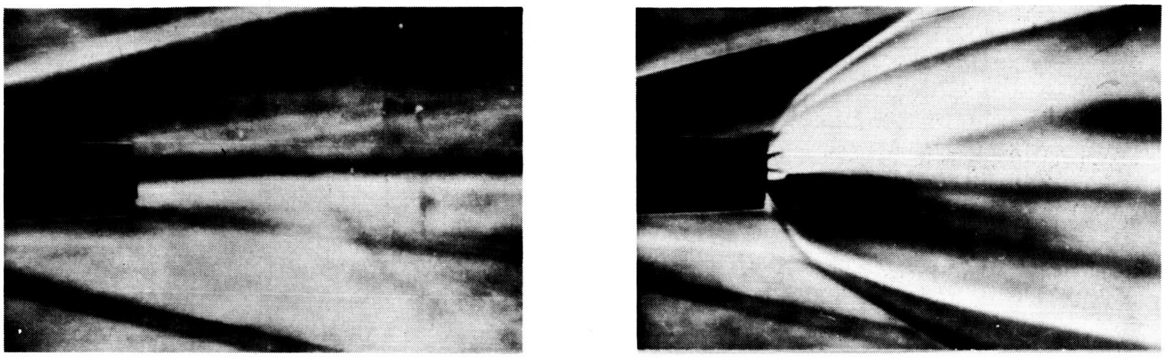

jet off

p_j/p_∞ = 475

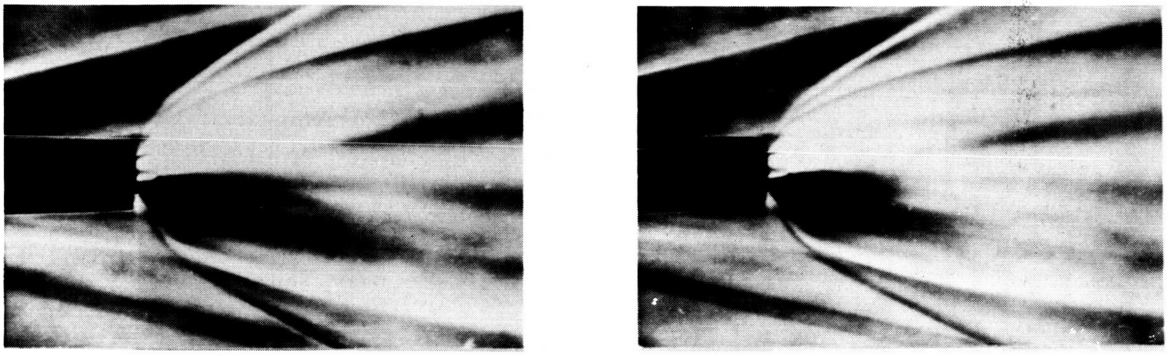

p_j/p_∞ = 390

p_j/p_∞ = 292

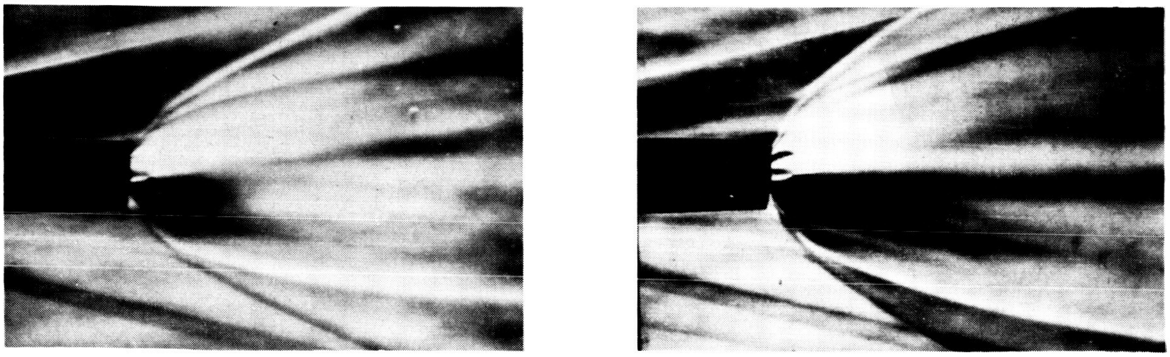

p_j/p_∞ = 195

no canopy, p_j/p_∞ = 520

(b) Nozzle A; $R = 1.20 \times 10^6$. L-59-5009

Figure 9.- Continued.

[redacted]

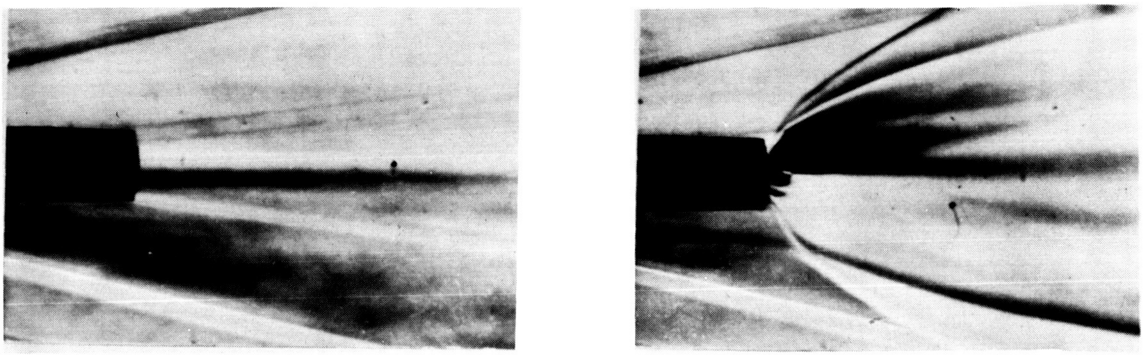

Nozzle A; jet off

Nozzle A; $p_j/p_\infty = 470$

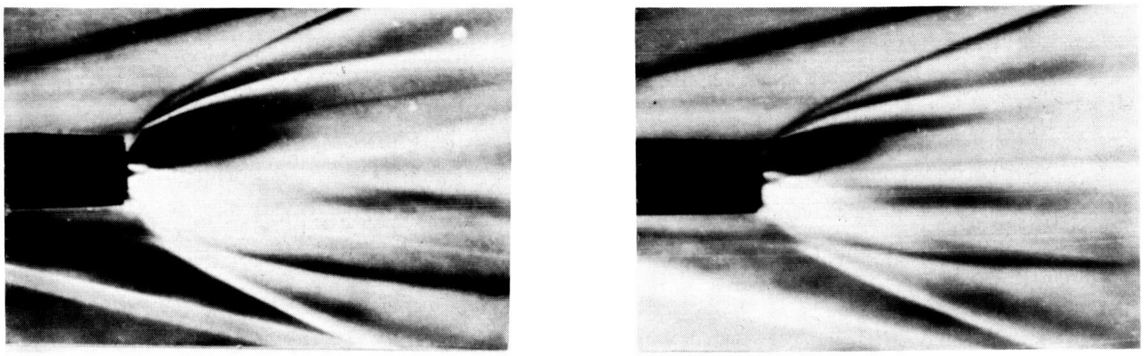

Nozzle A; $p_j/p_\infty = 203$

Nozzle A; $p_j/p_\infty = 100$

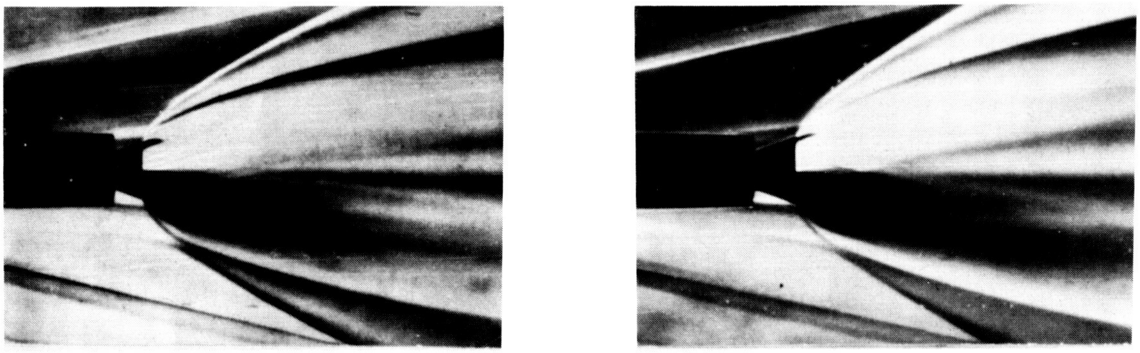

Nozzle B; $p_j/p_\infty = 170$

Nozzle C; $p_j/p_\infty = 139$

(c) $R = 2.05 \times 10^6$. L-59-5010

Figure 9.- Concluded.

[redacted]

[redacted]

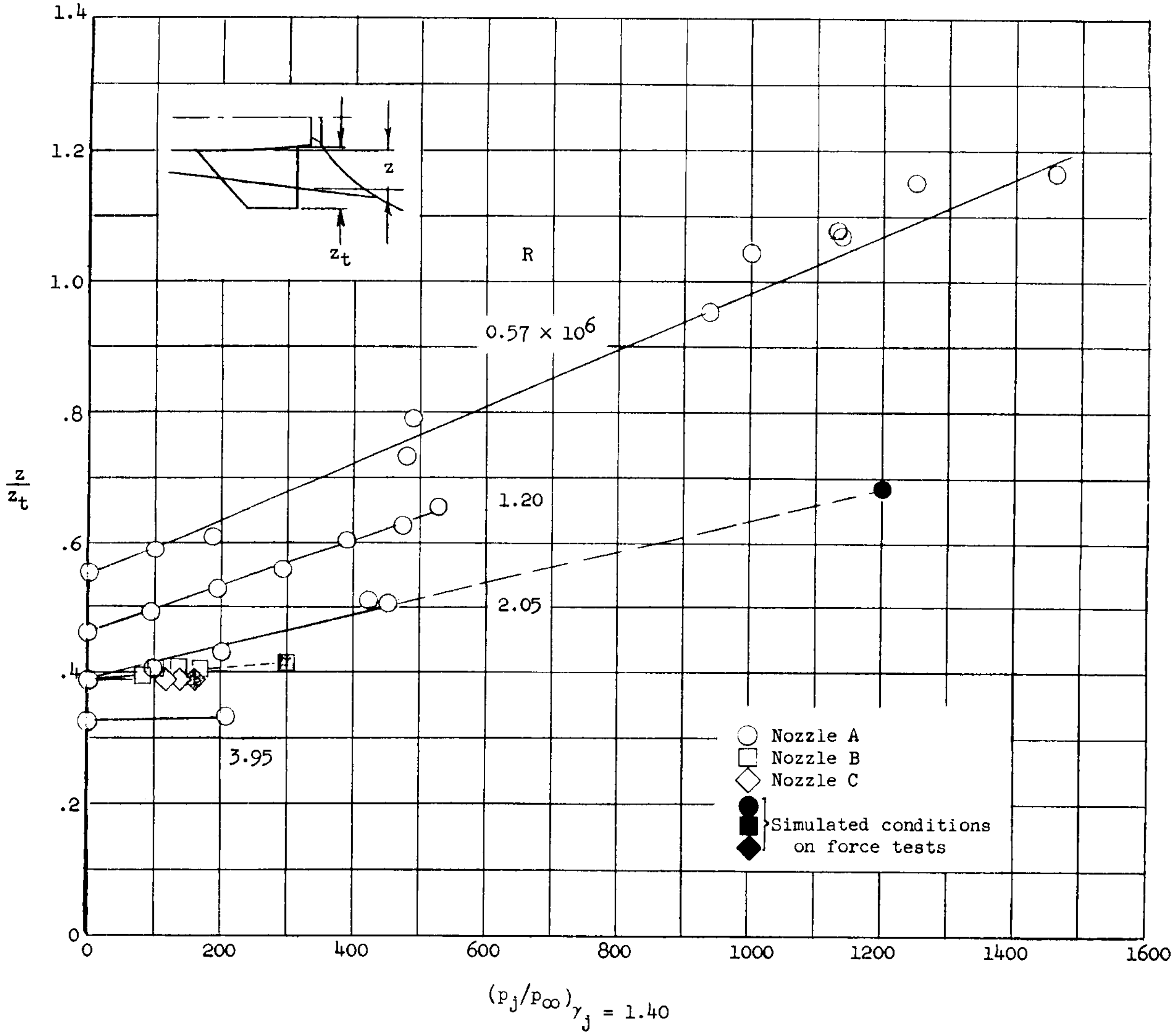

Figure 10.- Effect of jet-static-pressure ratio and Reynolds number on separated-flow region. $\alpha = 0^\circ$; $M_\infty = 6.86$.

[redacted]

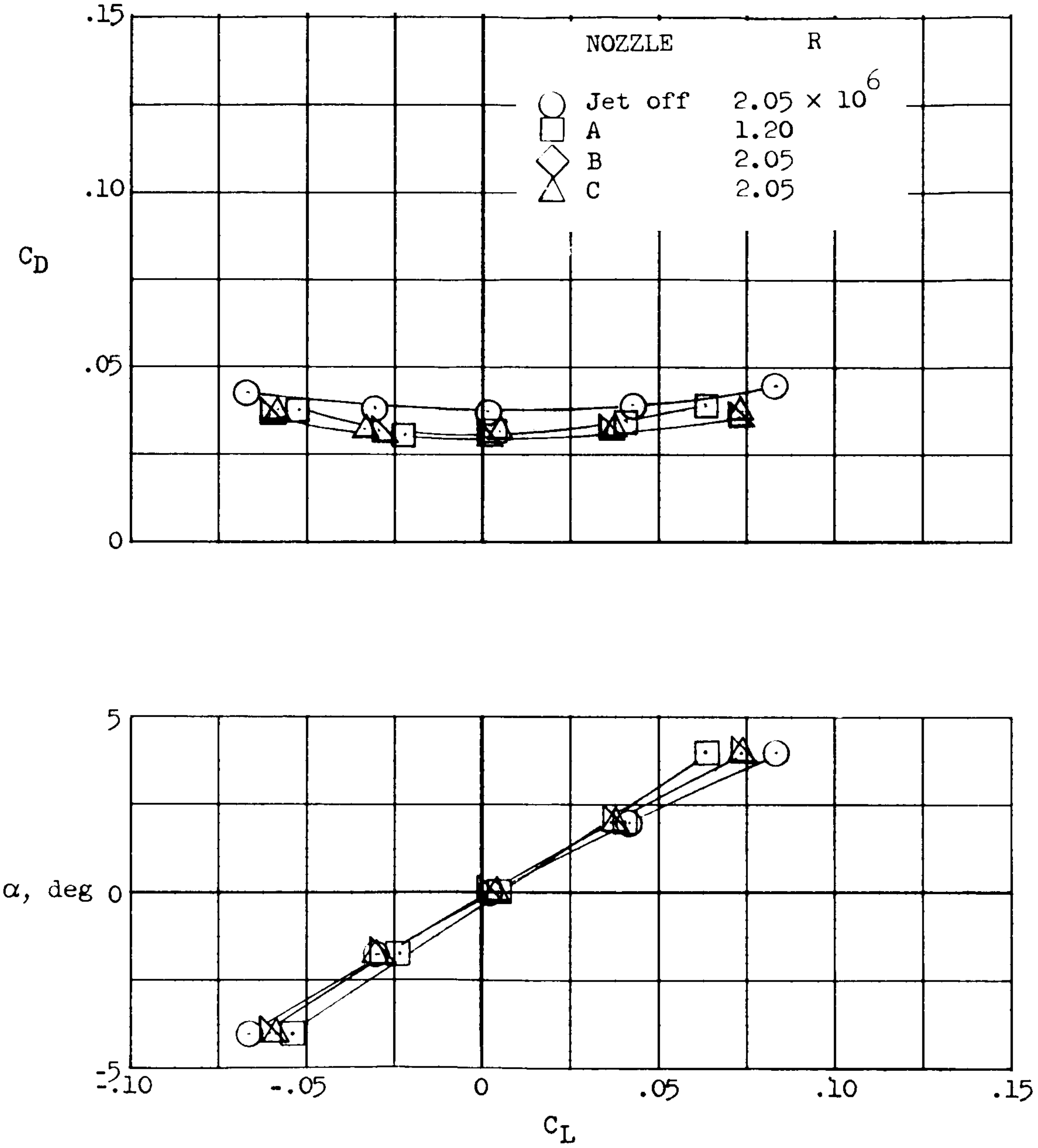

Figure 11.- Effect of simulated jet exhaust on lift and drag characteristics. $M_\infty = 6.86$; $\delta_h = 0^\circ$.

L-412

[redacted]

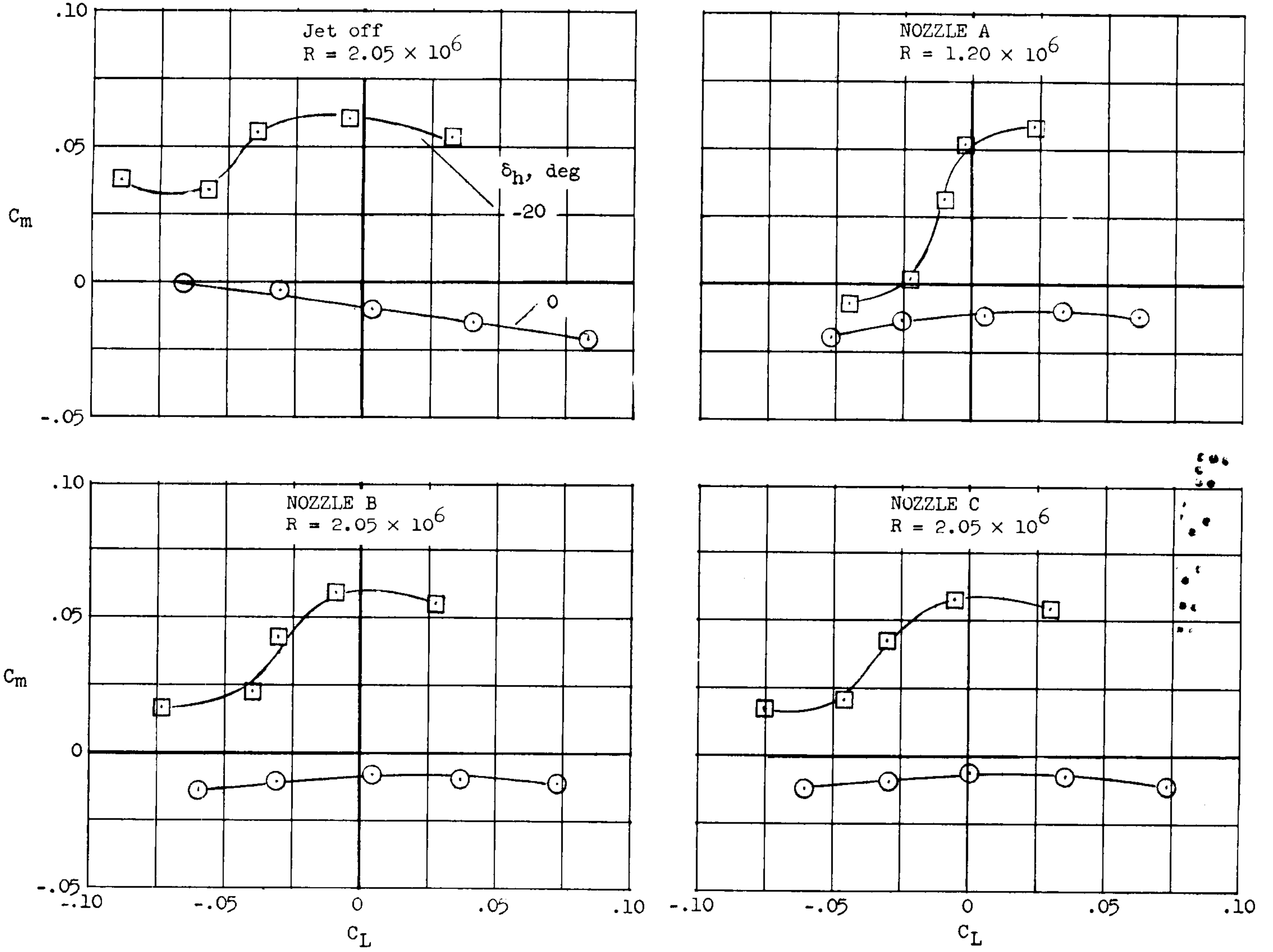

Figure 12.- Effect of simulated jet exhaust on longitudinal stability and control. $M_\infty = 6.86$.

[redacted]

[redacted]

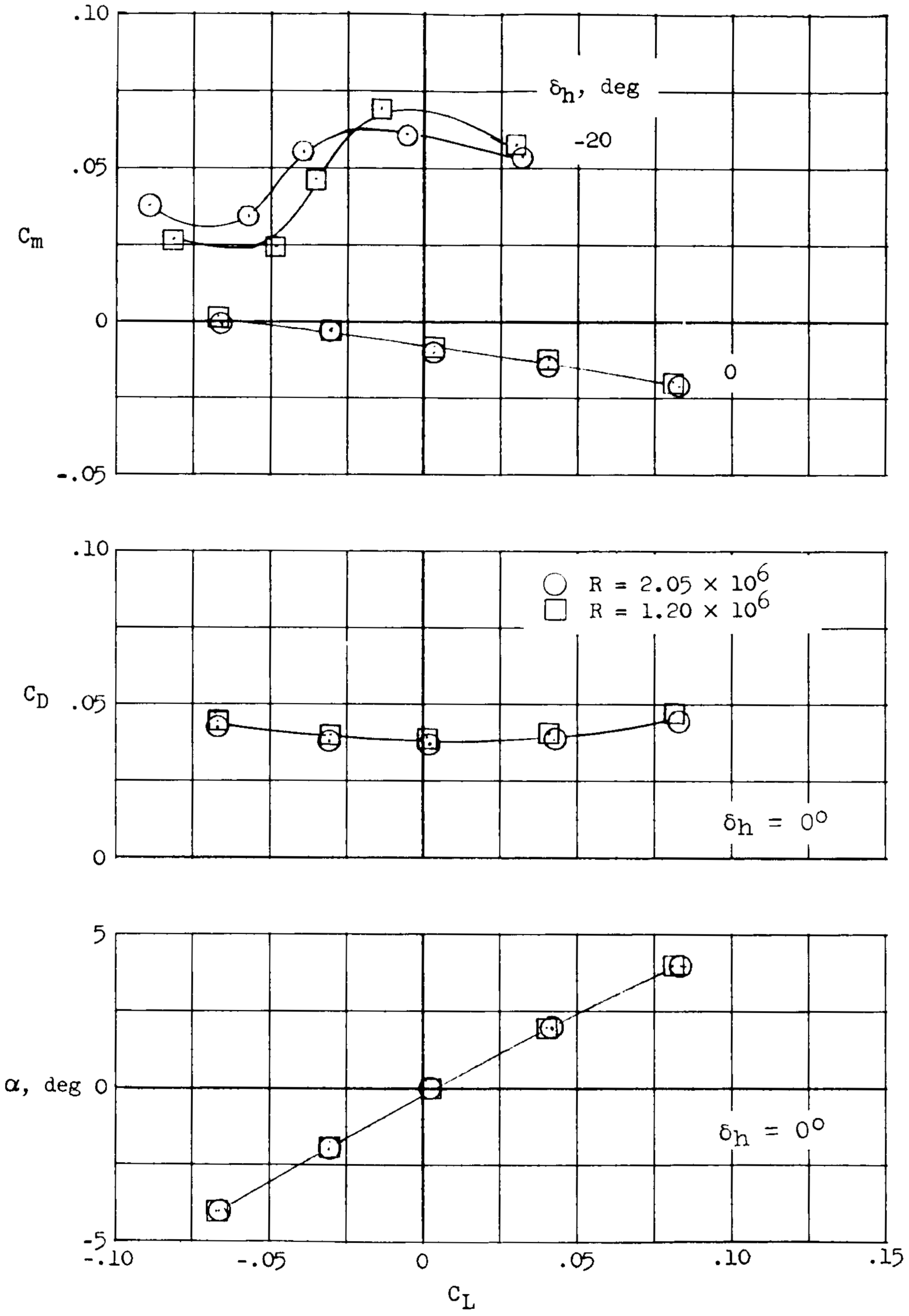

Figure 13.- Effect of Reynolds number on longitudinal characteristics of model with jet off. $M_\infty = 6.86$.

L-412

[redacted]

DECL[redacted]FIED

L-412

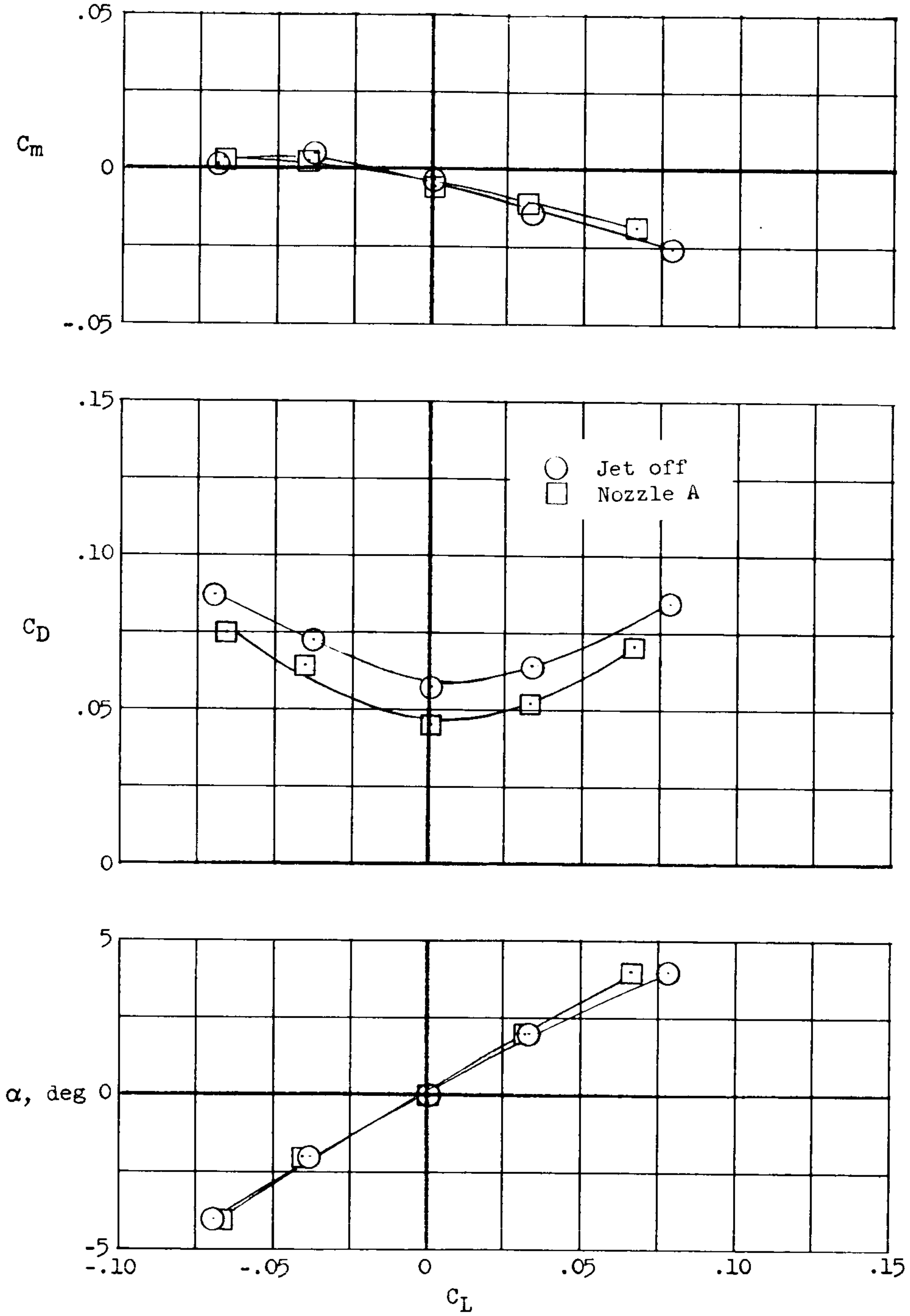

Figure 14.- Effect of simulated jet exhaust on longitudinal characteristics of the model with speed brakes deflected 35°. $M_\infty = 6.86$; $R = 1.20 \times 10^6$.

[redacted]

[redacted]

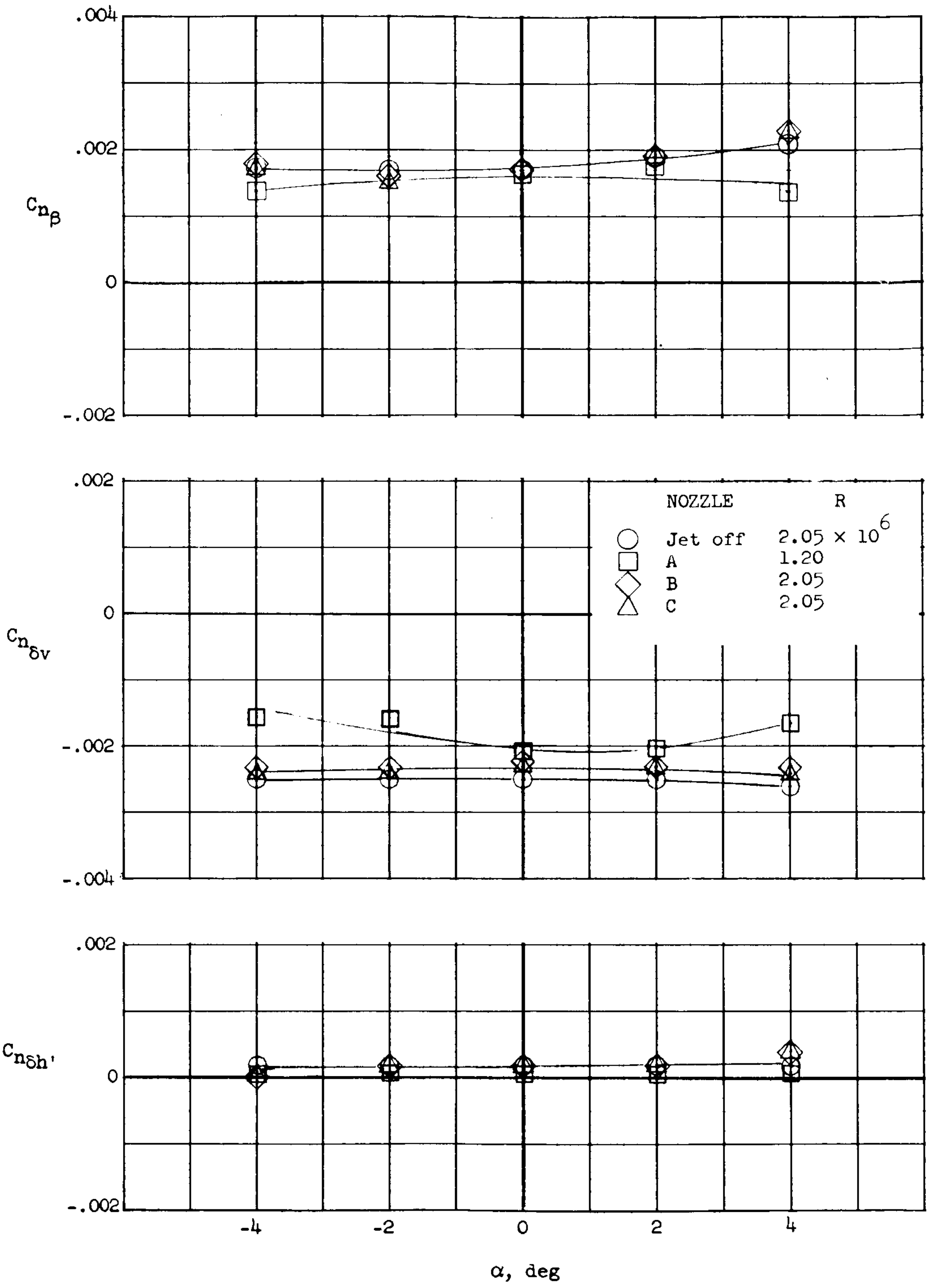

Figure 15.- Effect of simulated jet exhaust on directional stability and control. $M_\infty = 6.86$.

[redacted]

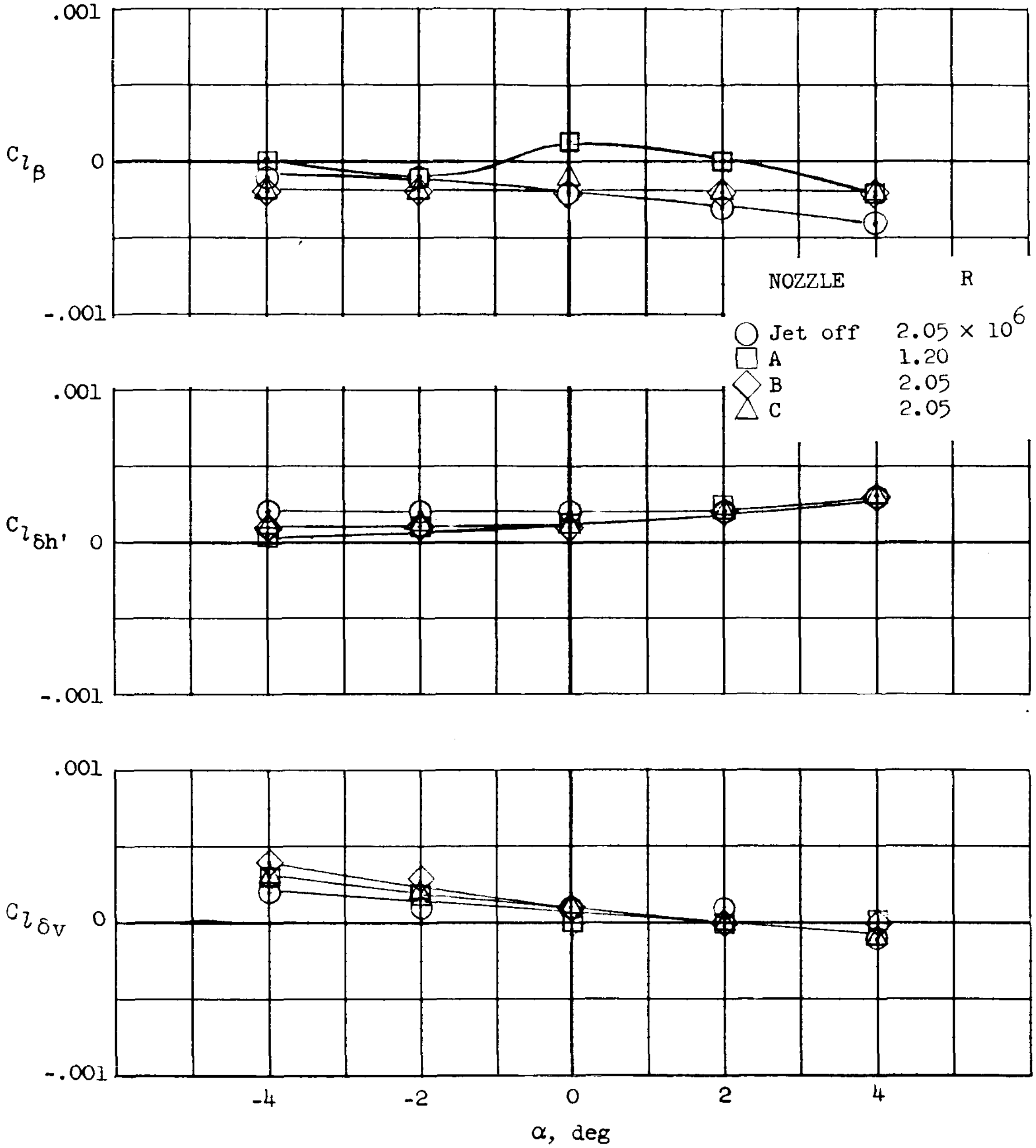

Figure 16.- Effect of simulated jet exhaust on lateral stability and control. $M_\infty = 6.86$.

[redacted]